Coupling of lattice dynamics and configurational disorder in metal deficient $Al_{1-\delta}B_2$ from first-principles

Erik Johansson, Fredrik Eriksson, Annop Ektarawong, Johanna Rosen, Björn Alling, et al.

View Online   **Export Citation**   **CrossMark**

ARTICLES YOU MAY BE INTERESTED IN

Energetics of boron near tungsten surfaces: A first-principles study
Journal of Applied Physics **130**, 015101 (2021); https://doi.org/10.1063/5.0053100

In-plane anisotropic electronic properties in layered α'–In_2Se_3
Journal of Applied Physics **130**, 015103 (2021); https://doi.org/10.1063/5.0050979

The quantum confinement effect on the spectrum of near-field thermal radiation by quantum dots
Journal of Applied Physics **130**, 015108 (2021); https://doi.org/10.1063/5.0049729
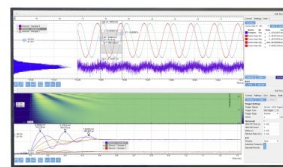
Coupling of lattice dynamics and configurational disorder in metal deficient Al$_{1-\delta}$B$_2$ from first-principles

Erik Johansson,[1,a] Fredrik Eriksson,[2] Annop Ektarawong,[3,4] Johanna Rosen,[2,b] and Björn Alling[1]

AFFILIATIONS

[1]Theoretical Physics Division, Department of Physics, Chemistry and Biology (IFM), Linköping University, SE-581 83 Linköping, Sweden

[2]Thin Film Physics Division, Department of Physics, Chemistry and Biology (IFM), Linköping University, SE-581 83 Linköping, Sweden

[3]Extreme Condition Physics Research Laboratory, Physics of Energy Materials Research Unit, Department of Physics, Faculty of Science, Chulalongkorn University, Bangkok 10330, Thailand

[4]Thailand Center of Excellence in Physics, Ministry of Higher Education, Science, Research and Innovation, 328 Si Ayutthaya Road, Bangkok 10400, Thailand

[a]Author to whom correspondence should be addressed: erik.johansson@liu.se
[b]Present address: Materials Design Division, Department of Physics, Chemistry and Biology (IFM), Linköping University, SE-581 83 Linköping, Sweden.

ABSTRACT

We investigate the role metal vacancies play in the phase stability and properties of Al$_{1-\delta}$B$_2$ using first-principles calculations, alloy theory simulations, phonon calculations, and experimental *in situ* x-ray diffraction measurements of thermal expansion. The relevant concentrations and configurations of metal vacancies are analyzed using cluster expansion and special quasirandom structure methods combined with vibrational free energy calculations within the quasiharmonic approximation for ordered and disordered phases. We find that electronic structure effects stabilize Al$_{1-\delta}$B$_2$ in a narrow composition range of $0.073 \leq \delta \leq 0.096$ depending only weakly on temperature while they destabilize ideal stoichiometric AlB$_2$. This composition corresponds to the narrow range $0.311 \leq x \leq 0.317$ in the formulation of Al$_x$B$_{1-x}$, which can explain the appearance of this phase as a line compound with the ideal AlB$_2$ stoichiometry in most phase diagrams. The ordered structures of vacancies found at low temperature are destabilized and disordered already at a low temperature of ~200 K. Our experiments observe linear thermal expansion coefficients $\alpha_a = 4.8 \times 10^{-6}$ K^{-1} and $\alpha_c = 10.85 \times 10^{-6}$ K^{-1} at room temperature. Only thermal expansion calculations of disordered phases compare well with these measurements, and, in particular, stoichiometric vacancy-free AlB$_2$ shows dramatic overestimations of the experimental thermal expansion. These results highlight the importance of disordered Al vacancies on both stability and vibrational properties of Al$_{1-\delta}$B$_2$.

I. INTRODUCTION

The hexagonal AlB$_2$-type crystal structure is often encountered in the large family of metal boride materials. It belongs to the P6/mmm hexagonal space group and is visualized in Fig. 1. As an example, MgB$_2$ is a well-known high-temperature superconductor,[1,2] and transition metal diborides like TiB$_2$ and ZrB$_2$ display high hardness, high elastic constants, good thermal and chemical stability, and electrical conductivity, making them relevant for hard cutting tools or protective coatings[3–6] and electrical contacts in harsh conditions.[7] AlB$_2$ itself is used to control solidification in aluminum alloys.[8] Recently, thin films of ternary diboride alloys in the AlB$_2$-type structure have been attracting attention for possible
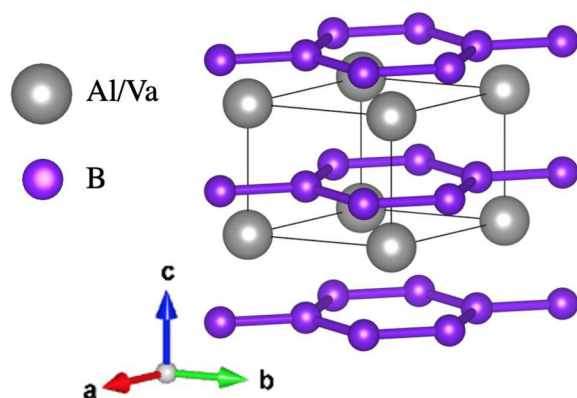
FIG. 1. The hexagonal unit cell of AlB_2. Each unit cell consists of one aluminum atom (gray) and two boron atoms (purple).

improvement of hard coating properties including the age-hardening phenomena, which have been predicted[9,10] and observed[11,12] in $Ti_{1-x}Al_xB_2$.

However, even though the crystal structure type is named after AlB_2, AlB_2 itself is, strictly speaking, not thermodynamically stable in stoichiometric form. It is instead known from experiments to be systematically understoichiometric on the Al metal sublattice and can be described as $Al_{1-\delta}B_2$. Here, δ is typically around 0.1 with a composition of $Al_{0.9}B_2$ being close to the reported average, while our literature search revealed an observed range from 0.07 to 0.122 depending on the synthesis method and conditions.[18] There is no clear evidence or report on whether or not the vacancy concentration is in fact variable, although the concern is also brought up by Sun *et al.*[16] Loa *et al.* calculated the electronic band structure and concluded that stoichiometric AlB_2 partially occupies antibonding Al-s states from the conduction band. They explained that a small fraction of Al vacancies is favored, as it optimizes the balance between filling bonding states of B–Al hybridization character and depleting the Al-s states.[13] Koch discussed the role of composition of Al vacancies on the total energy, structural relaxation, and electronic band structure of $Al_{1-\delta}$, finding $\delta = 0.13$ to be the static lattice equilibrium composition.[19]

Many questions regarding $Al_{1-\delta}B_2$ are still open: There is no consensus of the details of its composition stability range as a function of temperature in the literature. While the observation of Al understoichiometry is well established,[19] the phase diagram literature still suggests a line compound at the idealized AlB_2 composition,[20] highlighting that the stability limits with respect to Al-rich and B-rich competing phases are not well established. This is surprising, given the usage of $Al_{1-\delta}B_2$ in solidification of Al melts. Questions are also open regarding the configurational thermodynamics of Al-site vacancies. They might be configurationally disordered at high temperature, but thermodynamics dictate that at low temperature there should be ordered phases, at least theoretically stable, even if low diffusion might hinder their realization in practice. Furthermore, how the configurational disorder on the Al-sublattice couples to lattice vibrations is not known. The

possible importance of vibrational effects should not be ruled out because there is a presence of two light boron atoms for every lattice site with configurational disorder. To add to the uncertainty about this system, there is a lack of experimental and theoretical reports of the thermal expansion of $Al_{1-\delta}B_2$ as a function of temperature. These uncertainties slow down the development of novel AlB_2-based alloys as well as other metal diborides with the same crystal structure where off-stoichiometry might also be present.

In this work, we perform theoretical simulations, in particular, alloy theory simulations and lattice dynamics simulations based on the electronic structure theory to investigate the following outstanding questions for AlB_2: Which configurations of Al vacancies form stable structures with respect to the constituent elements, ideal stoichiometric AlB_2, and each other? What is the stable composition range for the compound as a function of temperature? Why is it reported to be narrow? What is the effect of lattice dynamics on stability and what is the effect of configurational order and disorder on lattice dynamics and thermal expansion? To compare with the latter, we performed *in situ* x-ray diffraction (XRD) measurements during heating of commercial AlB_2 powder to obtain the lattice constants of $Al_{1-\delta}B_2$ as a function of temperature.

II. METHODS

The theoretical framework is based upon first-principles density functional theory (DFT), which is used to derive the ground state electronic structure and total energy of the materials. Calculations are performed using the Vienna *Ab initio* Simulation Package (VASP),[21,22] with a plane wave approach using the Projector-Augmented-Wave (PAW) method.[23] The generalized gradient approximation (GGA) functional is used for calculating the exchange-correlation energies, as proposed by Perdew, Burke, and Ernzerhof (PBE96).[24]

To ensure a sufficient energy- and force-convergence, a plane wave energy cutoff of 600 eV is used for all structures. For the AlB_2 unit cell and all its defective vacancy structures, a k-point mesh of $15 \times 15 \times 15$ is used when sampling the Brillouin zone in the Monkhorst–Pack scheme,[25] and a $5 \times 5 \times 5$ mesh is used for the large supercell phonon calculations.

Equilibrium volume is obtained by first calculating the total energy for a set of fixed volumes, where cell shape and all atomic coordinates within the cell are allowed to relax. The data are then fitted to the third-order Birch–Murnaghan equation of state[26,27] upon which minimizing the total energy gives the equilibrium volume at zero pressure.

For electronic density of states (DOS) calculations, the tetrahedron method with Blöchl corrections[28] for Brillouin zone integrations was used, with similar Monkhorst–Pack **k**-point mesh sampling as when relaxing the different structures.

In this study, configurational disorder is modeled by the special quasirandom structure (SQS)[29] and cluster expansion (CE)-based procedures.[30] The SQS approach for disordered $(Al_{1-\delta}Vac_\delta)B_2$ vacancy structures ensures a good model for disordered vacancies on the metal sublattice. It distributes the metal atoms and vacancies in such a way that, on average, the short-range order parameters vanish on several close-ranged coordination shells. For comparison, different $Al_{1+y}B_2$ and $AlB_{2\pm z}$ structures with antisite, vacancy, and split-bond defects were also considered. In what follows, we will adapt the

Al_xB_{1-x} notation for easier comparison to experimentally available Al−B phase diagrams, where $x = (1-\delta)/(3-\delta)$, such that idealized AlB_2 ($\delta = 0$) takes on $x = 1/3$.

Cluster expansion (CE) formalism, as proposed by Sanchez *et al.*[30] and Connolly and Williams,[31] implemented in the Alloy-Theoretic Automated Toolkit (ATAT),[32] is used to derive a model that describes metal deficient AlB_2 structures. Training of the said model is done using structures generated using the algorithm by Hart and Forcade,[33] implemented in the MIT *Ab initio* Phase Stability (MAPS)[34] subroutine of ATAT. One thousand and forty-seven ordered Al_xB_{1-x} structures containing up to 25% metal vacancies and 50 atomic sites per primitive supercell unit cell were generated and relaxed using DFT calculations. The CE model with 800 structures included in the fit and containing 100 two-site, 100 three-site, and 10 four-site clusters was found satisfactory in describing the energies of both included and excluded structures. The maximum diameter (length of the longest pair within the cluster) is 20.8, 9.6, and 6.0 Å for two-, three-, and four-site clusters, respectively. The CE model fits the 800 input structures with the leave-one-out cross-validation score (CVS) of 2.43 meV/site and the 147 randomly excluded structures with the corresponding 2.20 meV/site.

The CE is used as the Hamiltonian in canonical Monte Carlo (MC) simulations, using the easy Monte Carlo code (EMC2)[35] subroutine implemented in ATAT. Simulation boxes of $16 \times 16 \times 13$ hexagonal primitive supercells (9984 atoms) are used. The simulations are performed at fixed vacancy concentrations, ranging from 0% to 25%, in steps of 2.5%, with the addition of 6.25%, 8.75%, 11.25%, and 13.75% for increased resolution near the 0 K convex hull. For each simulation, Al_xB_{1-x} starts in a disordered configuration at 6000 K and is cooled using simulated annealing, first to 2000 K using $\Delta T = 100$ K and then down to 0 K using $\Delta T = 25$ K. At each simulated temperature, the system is equilibrated with 20 000 steps and an additional 14 000 steps sample an average energy for evaluating thermodynamic quantities.

PHONOPY[36] is used to derive lattice vibration effects in both harmonic approximation (HA) and quasiharmonic approximation (QHA),[37–39] capturing the influence of both ordered and disordered vacancies at different concentrations on phase stability and thermal expansion of Al_xB_{1-x}. Finite displacements of 0.01 Å of the atoms from their equilibrium positions are performed using the Parlinski–Li–Kawazoe method.[40] For the vibrational study, two defective ordered Al_xB_{1-x} structures at different concentrations are considered. First, a 12.5% vacancy structure Al_7B_{16} is manually generated by removing the (0,0,0) Al atom from a regular $2 \times 2 \times 2$ AlB_2 supercell, and then extending two times in each direction arrives in a 184 atom defective supercell with vacancies in alternating layers. The second structure is the $2 \times 2 \times 2$ supercell of ordered $Al_{11}B_{24}$ primitive supercell, lying on the convex hull, containing 280 atoms. For disordered vacancies, two SQS structures are used: one $4 \times 4 \times 4$ (184 atoms) supercell with 12.5% vacancy structure and one $4 \times 4 \times 5$ (232 atoms) supercell with 10.0% vacancy structure. This ensures that the experimentally reported range of 7%–12.2% vacancies can be probed, and differences between the configurational order and disorder can be captured. For the pure elements as competing phases for Al_xB_{1-x}, a $4 \times 4 \times 4$ (256 atoms) supercell is used

for face-centered cubic (fcc) aluminum and a $3 \times 3 \times 3$ (324 atoms) supercell for α-rhombohedral boron.

Phase stability of Al_xB_{1-x} as a function of temperature is derived from the formation free energy, taken with respect to the constituent elements in equilibrium, fcc-Al and α-B, where the configurational free energy of the compound, with vacancy concentration $\delta = (3x-1)/(x-1)$, is taken from the MC simulations. It is expressed as

$$\Delta F^{MC}(\delta, T) = \Delta E^{MC}(\delta, T) - T\Delta S^{MC}(\delta, T), \quad (1)$$

where the configurational mixing entropy is obtained through downward thermodynamic integration from infinite temperature

$$\Delta S^{MC}(\delta, T) = \Delta S_{mix}^{MF}(\delta) + \int_{\infty}^{T} \frac{C_V(\delta, T')}{T'} dT'. \quad (2)$$

The first term is the mean field configurational entropy assuming vacancies are ideally disordered in the high-temperature limit,

$$\Delta S_{mix}^{MF}(\delta) = -k_B[\delta \ln(\delta) + (1-\delta) \ln(1-\delta)], \quad (3)$$

and the second term gives the temperature dependent entropy contribution from the canonical MC simulation box. For practical reasons, the integral from infinite temperature has to be truncated. Given the very high initial temperature of the MC simulation boxes, 6000 K is a suitable truncation such that the initial mixing entropy of the disordered state reduces to $\Delta S^{MC}(\delta, 6000 K) = \Delta S_{mix}^{MF}(\delta)$. We have checked that the CE Hamiltonian in the fully disordered limit modeled by MC simulations at artificial 60 000 K gives an energy within 1.22 meV/atom of the SQS values.

A. Experimental details

Commercially available AlB_2 powder (Sigma-Aldrich, Sweden AB) with particle sizes smaller than $44 \mu m$ was used. The reported composition was 48 mass% boron (for idealized pure AlB_2, boron is 44.5 mass%) and the rest being aluminum and impurities. X-ray diffraction measurements were performed on a Panalytical Empyrean diffractometer using a Cu x-ray tube, a parallel beam mirror with a $1/2°$ divergence slit and a 4 mm mask on the primary side, and a parallel plate collimator and a collimator slit (0.27°) on the secondary side, together with a PIXcel3D detector in 0D mode. The diffractometer was equipped with an Anton Paar DHS1100 heating stage and a graphite dome allowing diffraction measurements to be performed under a vacuum of 2×10^{-2} mbar at temperatures up to 1100 °C.

X-ray diffraction θ–2θ scans were measured in the range 31°–81° 2θ with a step size of 0.04°/step and a collection time of 3.5 s, giving a total measurement time of 25 min/scan. Measurements were made at room temperature and up to 1100 °C in steps of 100 °C. The sample height was aligned at $2\theta = 0°$ after each temperature increase, and an additional room temperature scan was performed after the annealing procedure.

The Panalytical Highscore software was used for phase analysis and profile fitting. In addition to diffraction peaks from the

AlB$_2$ phase, also Al$_2$O$_3$ and AlN diffraction peaks were recorded, where the AlN peaks originate from the AlN sample holder. For accurate peak positioning, the background was determined and peak profile fitting was performed using both Cu K$_{\alpha1}$ and K$_{\alpha2}$. A nonlinear least square method was used for the refinement of the hexagonal lattice parameters a and c.[41]

III. RESULTS

A. Electronic structure

The unit cell of AlB$_2$ ($P6/mmm$ symmetry) is presented in Fig. 1. It shows how the compound consists of alternating hexagonal metal and boron layers. Existing experimental and theoretical findings agree that metal vacancies are present, but little is said about other defects. Therefore, we start our investigation by considering a number of additional plausible types of defects in the host lattice, created in a $2 \times 2 \times 2$ supercell containing 24 atoms. For this starting point, the idea is not to explore the exact details of each defect, but rather capture the qualitative energy trend involved in their formation. Different antisite, vacancy, and interstitial defects are considered, and their formation energy is calculated through

$$E_{\text{defect}} = E^{\text{sc}}(\text{defect}) - E^{\text{sc}}(\text{no defect}) \pm \sum_i \mu_i N_i, \qquad (4)$$

where first two terms are the total energies of the supercell (sc) with and without the defect, and the last term corresponds to the defect that is formed by adding or removing N_i atoms of chemical potential μ_i. Some selected defects are visualized in Fig. 2(a), with their resulting defect formation energies being shown in Fig. 2(b).

In colored solid circles, both aluminum (green) and boron (purple) antisite defects are found to be energetically unfavorable. A number of boron interstitial positions were tested, with the most unfavorable position being the center of a boron hexagon, corresponding to the blue cross. The ones below represent different tilts of the split-bond boron dumbbell shown in the top left of Fig. 2(a). Boron interstitials are all deemed unlikely. Letting Al and B atoms exchange sites is found to be unfavorable. The purple open circle shows how boron vacancies are predicted to also have positive formation energy. The most unstable defect is found to be Al in an interstitial position, here relaxed into the center of a boron hexagon.

It is only the aluminum vacancy (green open circle) that has a negative formation energy of -66.22 meV/defect. The other defects may still be stabilized by temperature and entropy effects, but this initial sweep indicates that only metal vacancies are intrinsic in Al$_x$B$_{1-x}$. Again, these defective structures do not necessarily represent optimal configurations, but they do serve an illustrative purpose. As such, we move on to consider the boron sublattice being fully occupied and assuming a spectator role, and in terms of defects, the focus is shifted solely onto metal vacancies; their configuration, concentration, and impact on phase stability and thermal expansion.

In contrast to the defective structures shown in Fig. 2, the structures to be considered in the following analysis will have vacancies ordered in practically every way, at each considered concentration, such that the most optimal configurations can be investigated.

Stability of metal deficient Al$_x$B$_{1-x}$ structures is now studied by calculating the formation energy as a function of composition,
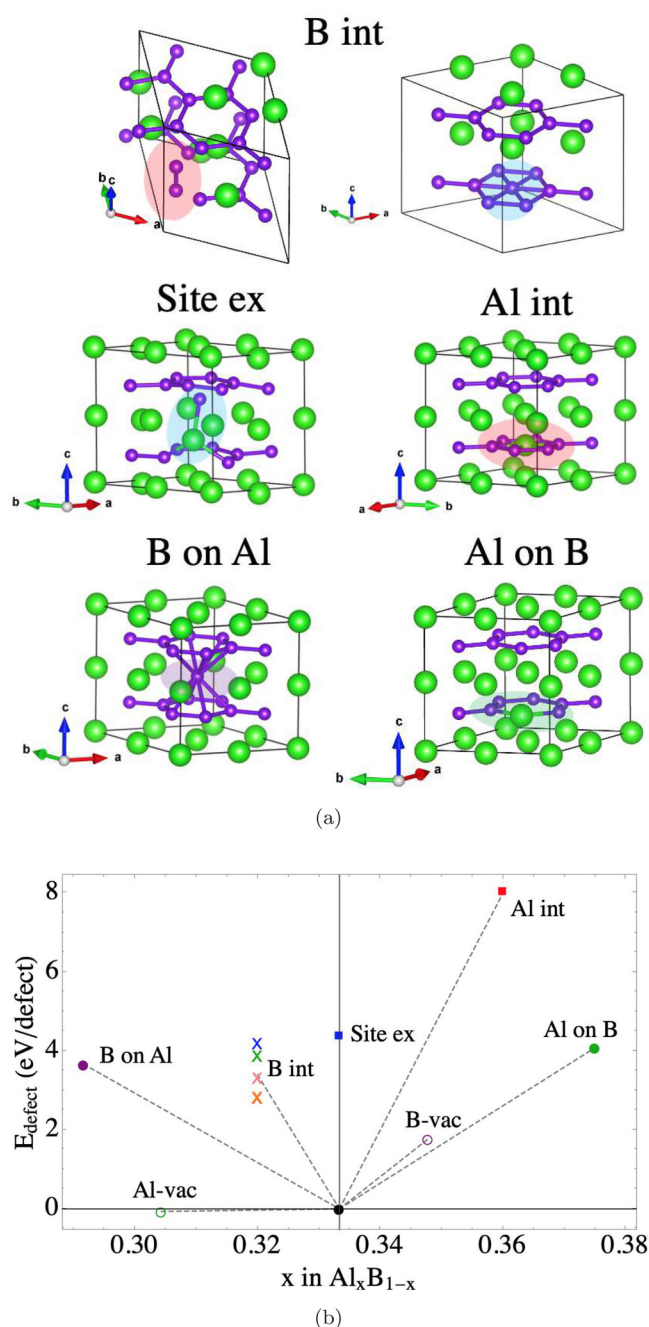

(a)

(b)

FIG. 2. Investigation of potential defects in AlB$_2$. (a) Visualization of some of the considered defects. Purple and green spheres represent boron and aluminum, respectively. (b) Formation energies of defects created in an ideal $2 \times 2 \times 2$ AlB$_2$ supercell (black circle). Colored solid circles are antisite defects; green is when Al sits on a B site and purple is the reverse case. Open circles are vacancy defects; green is an Al vacancy and purple is a B vacancy. Crosses correspond to different B interstitials. The blue square corresponds to site exchange of Al and B. The red square marks Al in an interstitial position.
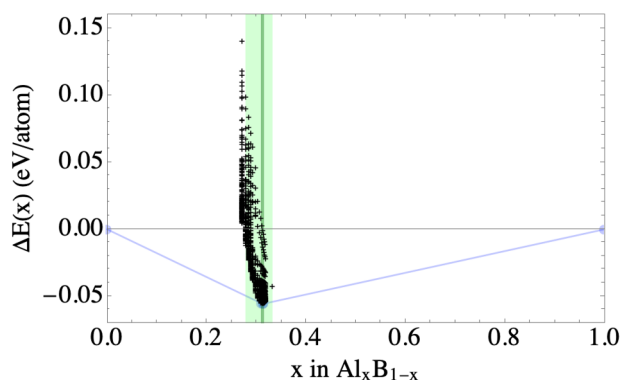
FIG. 3. Formation energy of $Al_{1-\delta}B_2$ calculated with DFT, as a function of aluminum composition, x in Al_xB_{1-x}. Black crosses correspond to MAPS-generated structures. The green shaded area shows where $Al_{1-\delta}B_2$ is stable with respect to its constituent elements, but only the darker shaded stripe is where $Al_{1-\delta}B_2$ is part of the convex hull.

with respect to the pure constituent elements fcc-Al and α-B in equilibrium, via

$$\Delta E(x) = E(Al_xB_{1-x}) - xE(\text{fcc-Al}) - (1-x)E(\alpha-B). \quad (5)$$

Figure 3 displays this quantity for the 1047 Al_xB_{1-x} structures derived with DFT. Every black cross corresponds to a different structure, with a vacancy concentration of 0%–25%. Each considered concentration has around 100 structures, each with a different vacancy configuration. The green shaded area shows the narrow composition range, $0.280 \leq x \leq 0.333$, for which Al_xB_{1-x} vacancy structures are stable with respect to pure fcc-Al and α-B, with $\Delta E(x) \leq 0$, and the darker green area, the even more narrow region, constitutes the convex hull at 0 K, $0.310 \leq x \leq 0.315$.

From what our calculations predict, Al_xB_{1-x} structures with 25% vacancies are all unstable. The blue curve is the 0 K convex hull. As the stability region is so narrow, it is instructive to have a closer look. Figure 4 presents a magnification of the green area of interest shown in Fig. 3.

Here, open green circle corresponds to the manually created Al-vacancy structure that was previously presented in the bottom left of Fig. 2(b). Two disordered SQSs with 10.0% and 12.5% vacancies are shown in orange circles. It is interesting to compare the energies between ordered and disordered vacancies, and as one should expect, order is favored at 0 K. The $Al_{0.9}B_2$ SQS lies 10.74 meV above the convex hull, and the $Al_{0.875}B_2$ is 13.89 meV above. Looking at the Materials Project database,[42] the only reported stable Al–B structure (other than AlB_2) is $Al_{23}B_{50}$ (8% ordered vacancies, ID: mp-530274), represented by the sole red cross. As this structure's primitive supercell contains 73 atoms, it was not found in our scans of up to 50 atoms per primitive supercell. However, from our recalculations, this crystal structure is in fact not predicted to be on the 0 K convex hull, albeit being only 0.415 meV/atom above. We acknowledge its existence so close to the convex hull, but the structure is not investigated further in our
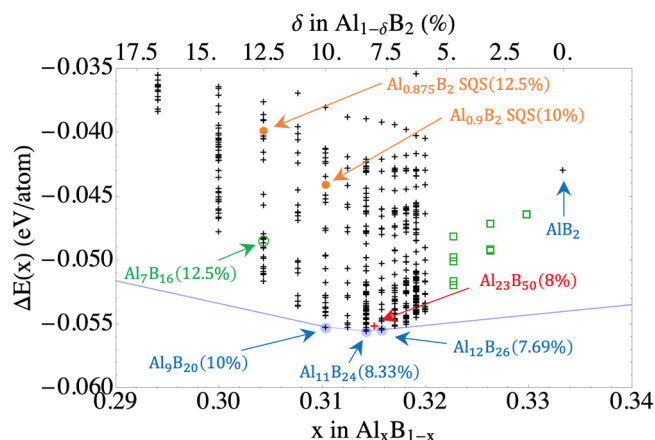

FIG. 4. Formation energy of $Al_{1-\delta}B_2$, as a function of aluminum composition, x in Al_xB_{1-x}. Black crosses correspond to MAPS-generated structures. Shaded blue circles highlight the structures on the convex hull. Open green circle represents the manually created Al-vacancy structure Al_7B_{16}, previously shown in Fig. 2(b). Solid orange circles correspond to the two SQSs with 10% ($Al_{0.9}B_2$) and 12.5% ($Al_{0.875}B_2$) vacancies. Red cross represents $Al_{23}B_{50}$ from Materials Project, discussed below. Open green squares correspond to manually created low-concentration structures with 1/64, 2/64, and 3/64 vacancies and are added for completion to bridge the gap. Their energies are above the convex hull as they are out-competed by the stable vacancy-richer $Al_{1-\delta}B_2$ structures in combination with pure Al.

work. The details of configurational disorder will be discussed in this subsection and in Sec. III D.

From calculating the 1047 structures using DFT, three vacancy structures, highlighted with arrows and blue circles in Fig. 4, are predicted to lie on the 0 K convex hull as ground states. They are hereafter denoted by the number of Al and B atoms in their primitive supercell and are given the names Al_9B_{20} ($\Delta E = -55.22$ meV/atom, 10% vacancies), $Al_{11}B_{24}$ ($\Delta E = -55.53$ meV/atom, 8.33% vacancies), and $Al_{12}B_{26}$ ($\Delta E = -55.42$ meV/atom, 7.69% vacancies). Meanwhile, as evident from Fig. 4, stoichiometric AlB_2 itself has a formation energy $\Delta E = -42.93$ meV/atom and lies 11.07 meV/atom *above* the convex hull. This explains the experimental findings of off-stoichiometry in AlB_2 samples.

The 0 K convex hull crystal structures are displayed in Fig. 5(b), where to the left, isolated top views of metal sublayers are chosen to highlight the vacancy configuration, as well as having the side view shown, to the right. Common to all three structures, vacancies lie in straight line formations that propagate throughout the metal sublayer, seen from the top view.

Looking from the side perspective, one can see that the vacancy lines are alternatively shifted, forming a zig-zag pattern between interplanar nearest-neighboring (nn) vacancy lines. The in-plane distance between vacancies and their neighboring vacancy lines varies with vacancy concentration. From top to bottom in Fig. 5(b), Al_9B_{20} has a *nn* distance between two vacancies of 6.01 Å, and the distance between two adjacent in-plane vacancy lines is 13.11 Å. Similarly, $Al_{11}B_{24}$ has distances of 7.96 and 12.03 Å, while $Al_{12}B_{26}$ has 7.96 and 13.11 Å. In each structure, a vacancy is
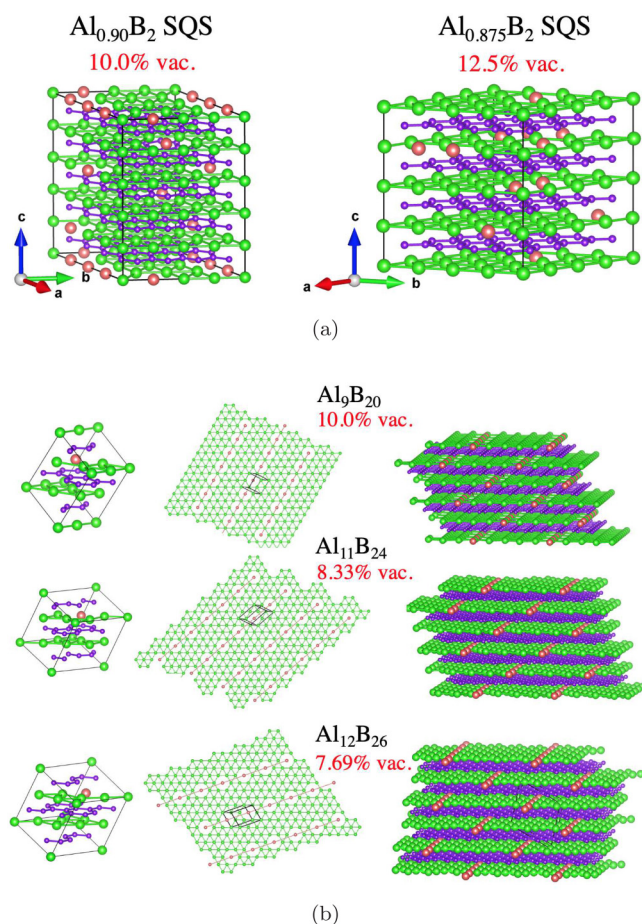
FIG. 5. Visualization of selected relevant structures. Purple, green, and red spheres represent boron, aluminum, and Al vacancies, respectively. (a) Two considered SQSs with 10.0% (left) and 12.5% (right) disordered vacancies. (b) Primitive supercell (left), top (middle), and side (right) view of the crystal structure of the three ordered defective AlB$_2$-type structures that lie on the 0 K convex hull. Black boxes in the top view correspond to the primitive supercells.
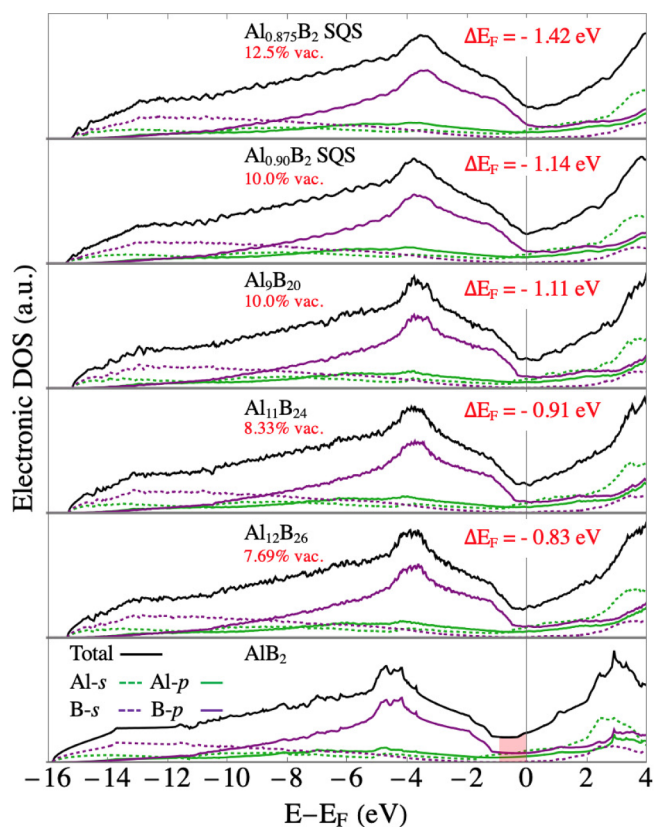

FIG. 6. Calculated electronic DOS, in arbitrary units, of AlB$_2$, the three ordered defective AlB$_2$-type structures on the 0 K convex hull, and two disordered SQSs. The energies are given with respect to the Fermi energy E_F of each structure, while the shift in E_F relative to AlB$_2$ is given in the legend. Black solid line is the total DOS, and the colored solid lines are the p-orbital contribution from aluminum (green) and boron (purple). Dashed colored lines are the s-orbital contributions to the DOS.

surrounded by an aluminum hexagon. For Al$_9$B$_{20}$, the *nn* vacancies have overlapping of such aluminum hexagons that share vertices. Both Al$_{11}$B$_{24}$ and Al$_{12}$B$_{26}$, having the same vacancy *nn* distance of 7.96 Å, have their corresponding closest hexagon vertices separated by one lattice spacing.

The difference here is rather the angle in which the vacancy line cuts the plane. For pedagogical purposes, an attempt has been made to horizontally align the bottom of the hexagonal edges, for all of the structures in Fig. 5(b). Then, if one defines the aforementioned angle as the deviation from this horizontal line, it turns out that Al$_{12}$B$_{26}$ has an angle of 19.11°, Al$_{11}$B$_{24}$ has 40.89°, and Al$_9$B$_{20}$ has 60.00°, that is, the in-plane vacancy line tilt increases with vacancy concentration for these structures on the 0 K convex hull.

To gain an understanding why metal vacancies are intrinsic and energetically favorable in Al$_{1-\delta}$B$_2$, and not only induced by entropy at high temperature, we calculate the electronic DOS.

The electronic DOS of the stoichiometric AlB$_2$ unit cell, the three ground state primitive supercells, lying on the 0 K convex hull, and two disordered vacancy structures is presented in Fig. 6. Black curves are the total electronic DOS, while purple corresponds to boron and green to aluminum. Dotted colored lines show the summed up s-orbital contribution of the respective atomic species, and solid colored lines show that of the p-orbitals. Boron has a Pauling electronegativity of 2.04 and aluminum 1.61, meaning boron will attract 3p and 3s electrons from aluminum. Consequently, the aluminum atoms contribute weakly to the total electronic DOS in Fig. 6.

For AlB$_2$, one can observe a pseudogap, a deep valley below the Fermi energy E_F, in the electronic DOS. This feature typically indicates that the bonding valence bands are completely filled. In the work of Vajeeston et al.,[43] it was concluded that the most significant contributor to the creation of such a pseudogap is the B (p)–B(p) covalent interaction. Furthermore, as hinted by Loa et al.,[13] the electronic band structure of AlB$_2$ reveals that π-type

bands, coming from B(p_z) states, and antibonding conduction bands with Al-s character near the gamma point are partially filled and give rise to the metallic state around the Fermi energy E_F. They go on to discuss, within a rigid-band model, that a 10% deficiency of aluminum would remove 0.3 valence electrons (as each Al has two 3s and one 3p valence electrons) and lower E_F by 0.9 eV. This results in complete depletion of the shallow-lying antibonding Al-s character states present near E_F in ideal AlB$_2$. Inspired by Loa *et al.*,[13] the above statement is visualized by shading the total electronic DOS of AlB$_2$ from the Fermi level down to 0.9 eV below, where Al$_{0.9}$B$_2$ is predicted to have its E_F. In their findings, it is this red region that contains partially filled antibonding bands of Al-s character.

In this work, with explicit treatment of vacancies in optimal configurations, we go beyond predictions and calculate the electronic DOS of defective AlB$_2$ structures. As presented in Fig. 6, the main characteristic of the defective structures is that the Fermi energy E_F has been shifted to the bottom of the pseudogap. This is most distinguishable for Al$_9$B$_{20}$, Al$_{11}$B$_{24}$, and the Al$_{0.90}$B$_2$ SQS. For disordered Al$_{0.875}$B$_2$, the Fermi level is slightly to the left of the pseudogap, indicating that vacancy concentrations higher than 12.5% will start depleting favorable bonding orbitals. This is in line with the quickly increasing ΔE of such structures in Fig. 4, regardless of configuration. The exact shift in the Fermi energy ΔE_F, relative to stoichiometric AlB$_2$, is -0.83 eV for Al$_{12}$B$_{26}$, -0.91 eV for Al$_{11}$B$_{24}$, -1.11 eV for Al$_9$B$_{20}$, -1.14 eV for the Al$_{0.90}$B$_2$ SQS, and -1.42 eV for the Al$_{0.875}$B$_2$ SQS.

To further this analysis, Fig. 7(a) shows the electronic band structure of ideal stoichiometric AlB$_2$. The red band represents the partially occupied antibonding conduction band with Al-s character, and in blue is the highest occupied valence band with B-p character. Figure 7(b) is a magnification of the region just below E_F, where the presence of conduction bands with Al-s (red) and B-p (black) characters is clearly seen. The shaded red region represents the prediction by Loa *et al.* that lowering the Fermi energy by 0.9 eV will deplete the shallow Al-s states around Γ. The primitive supercells of the defective structures in Fig. 6 do not have the hexagonal symmetry of AlB$_2$, making it difficult to explicitly calculate the band structure along high-symmetry lines.

However, the green dashed lines correspond to their E_F relative to AlB$_2$ such that a qualitative picture within a rigid-band model can be obtained. For Al$_{12}$B$_{26}$ (7.69% vacancies) with a relative shift of $\Delta E_F = -0.83$ eV, one sees that it is not enough to deplete the shallow Al-s states around Γ. Consequently, similarly to AlB$_2$ as shown in the electronic DOS, E_F of Al$_9$B$_{26}$ is located to the right of the pseudogap bottom. For Al$_{11}$B$_{26}$ (8.33% vacancies), with $\Delta E_F = -0.91$ eV, the shallow states are depleted, but E_F can be further shifted before reaching the highest occupied valence state located along $K - \Gamma$. For the last structure on the convex hull Al$_9$B$_{26}$ (10.0% vacancies), with $\Delta E_F = -1.11$ eV, some of the bonding valence states have been emptied, but it is balanced by further depletion of antibonding states. This balancing is reflected by its E_F being located precisely at the bottom of the pseudogap in the electronic DOS. The case is similar for the disordered Al$_{0.90}$B$_2$ SQS. Meanwhile, for $\Delta E_F = -1.42$ eV of the Al$_{0.875}$B$_2$ SQS, too many preferable bonding states start to be emptied, and all structures at this composition fall above the convex hull.
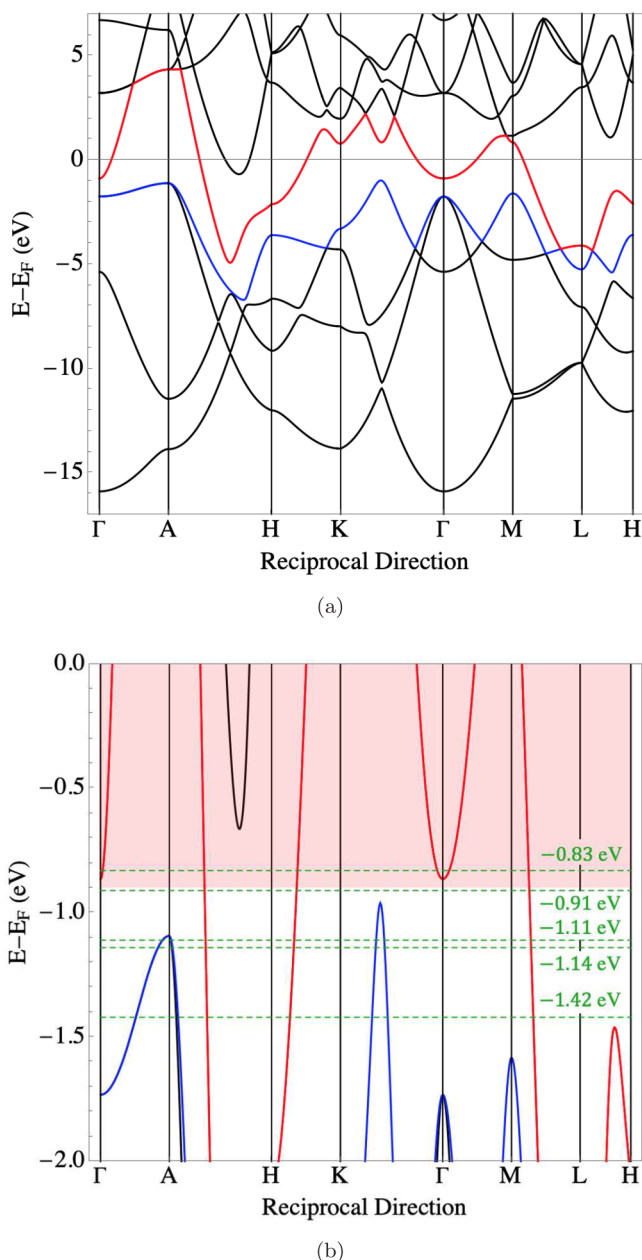

(a)

(b)

FIG. 7. Electronic band structure of stoichiometric AlB$_2$ along high-symmetry lines.

These calculations, in line with the rigid-band model prediction of Loa *et al.*, show that the metal vacancies in Al$_x$B$_{1-x}$ indeed can deplete overfilled antibonding molecular orbitals from the conduction band and stabilize the system energetically.

It is now clear that vacancy-mediated stabilization can be understood by average band-filling effects. In order to gain an
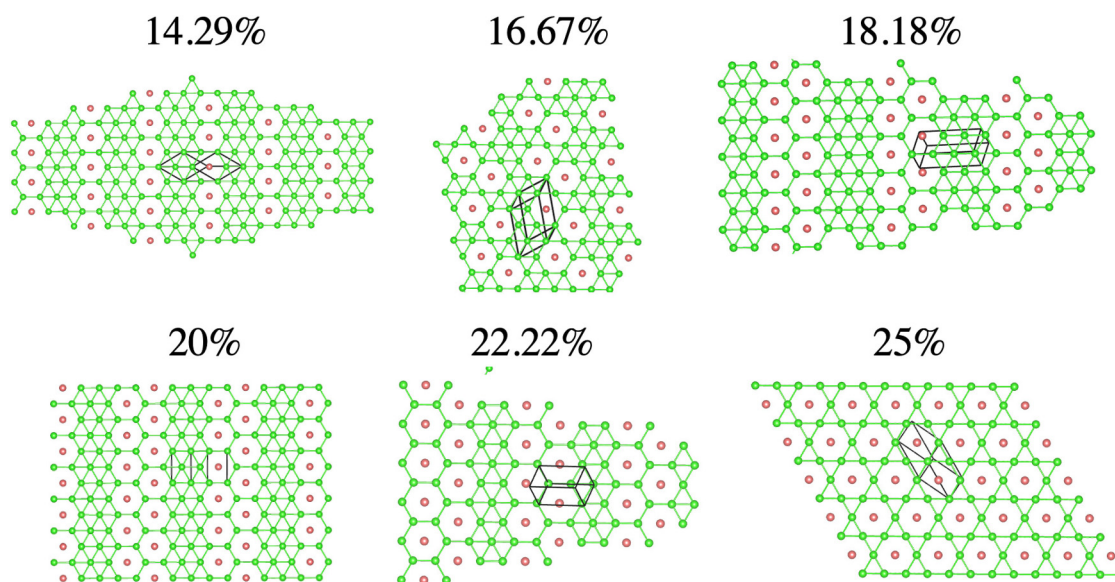
FIG. 8. The most stable $Al_{1-\delta}B_2$ structures for a subset of vacancy concentrations. Black boxes correspond to the primitive supercells. Green and red spheres represent aluminum and Al vacancies, respectively.

appreciation of what the vacancy configurations look like at concentrations higher than 10%, Fig. 8 shows isolated Al layers of the defective primitive supercell structures corresponding to the most stable ones in Fig. 4, at their respective concentrations.

Going from 14.29% vacancies, one sees a transition from single vacancy lines, common to all convex hull structures, to the formation of double lines at 18.18% that become more densely packed with increasing vacancy concentration. At 25%, the double lines become joined, effectively replacing every metal atom at the center of each hexagon with a vacancy. The destabilization that follows from having more than 10% vacancies is already understood from average band-filling arguments but is with this visualization made more clear through the emergence of more and more dangling Al bonds.

B. Cluster expansion

In the following steps, the 1047 ordered Al_xB_{1-x} structures, and their corresponding DFT energies, will be used to train a CE model that can predict total energies of different local vacancy configurations. Figure 9 presents the formation energies of all ordered structures. As the region of interest remains close to the convex hull (blue lines), a formation energy cutoff was set to include all structures with $\Delta E(x) \leq 0.03$ eV/atom, with respect to pure elements, in order to not focus the expansion on high energy features of low practical relevance. Thus, the highly unstable structures (red crosses) are excluded from the fit and 947 structures remains. As a complement to the often conventional "leave-one-out" CVS method, in this work, we extend upon this procedure and calculate a separate score based entirely on structures excluded from the CE. Therefore, out of the initial 947 accepted structures, a subset of 147 structures (green

crosses) were randomly excluded as a test data set, leaving 800 structures (blue crosses) to be included in the fit. This additional CVS ensures that the cluster expansion gives good prediction of the formation energies in the targeted area of interest, close to the convex hull.

Furthermore, the CE basis functions were selected in such a way that the CVS of the 147 random excluded structures was
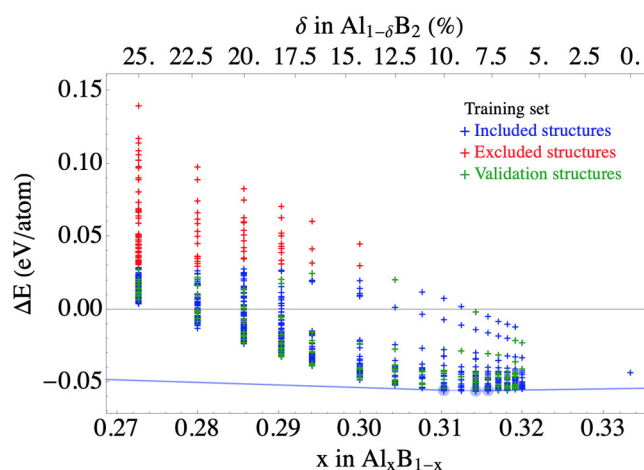

FIG. 9. Formation energies from DFT calculations of all MAPS-generated ordered Al_xB_{1-x} structures. Blue crosses show the structures that are included in the CE fit, while the red are the cutoff structures with $\Delta E(x) > 0.03$ eV/atom with respect to pure elements and in green are 147 randomly excluded structures, out of the initial 947 accepted structures, used for CE validation.

minimized. The search was initiated using a low number of pair interactions, and then systematically increasing, as well as adding higher order cluster interactions. It was found that a CE with 100 pair interactions, 100 three-site cluster interactions, and 10 four-site cluster interactions was satisfactory in predicting energies of excluded Al_xB_{1-x} structures, giving the conventional $CVS = 2.43$ meV/site and $CVS^{147rnd} = 2.20$ meV/site for the 147 random structures not included in the fit.

The effective cluster interactions (ECIs), as a function of length of the longest pair within the cluster, of this CE are presented in Fig. 10(a). Black circles show pair interactions, green triangles are triplets, and red diamonds are quadruplets or four-site cluster interactions. The strongest ECI contributions are from clusters having first-, second-, and third-nearest neighbor distance as the longest pair. The ECI magnitude decays to zero with respect to increasing cluster diameter and total number of sites included in the cluster. As such,

neither adding more pairs, triplets, or quadruplets nor introducing clusters with five or more sites would significantly improve the CE.

The predictive power can be visualized by plotting the fitted and predicted formation energies of the CE against DFT calculated values, as in Fig. 10(b). Here, perfect agreement $\Delta E_{CE} = \Delta E_{DFT}$ corresponds to the solid black line. The poor prediction of the 100 highly unstable structures in red is to be expected, as the choice of basis functions was intended to predict the 147 randomly excluded configurations (green crosses). Those and the fitted structures in blue lie virtually on top of the black line, which is reflected by their low validation scores.

C. Canonical Monte Carlo simulations

Being interested in the thermodynamics of vacancy ordering effects, the CE is hereafter used as the governing Hamiltonian for canonical MC simulations. This extends the modeling beyond 0 K ordered configurations into finite temperatures with interplay between configurational order and disorder. In this work, we also go one step further by also including vibrational contributions to the total free energy in both HA and QHA. To be shown later, at concentrations close to the 7%–12% range, vacancies are predicted to undergo a transition from ordered to disordered at temperatures above 200 K. Therefore, among the pure elements α-B ($x = 0.0$) and fcc-Al ($x = 1.0$), the two SQSs with 10% ($x = 0.310$) and 12.5% ($x = 0.304$) vacancies are used for phonon calculations, and quadratic interpolation between the points is employed to approximate the vibrational contribution across the entire compositional range. By using the disordered structures, we should get a reasonable $\Delta F_{vib}^{(Q)HA}(x, T)$ at all relevant temperatures. Three approximations of $\Delta G(x, T)$ are investigated and presented in Fig. 11 at temperatures of
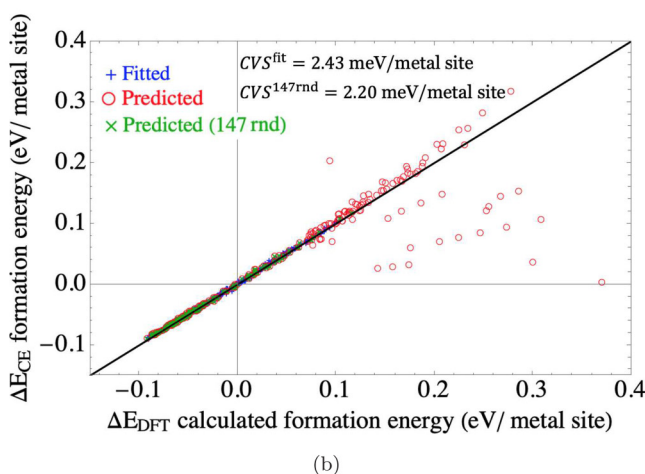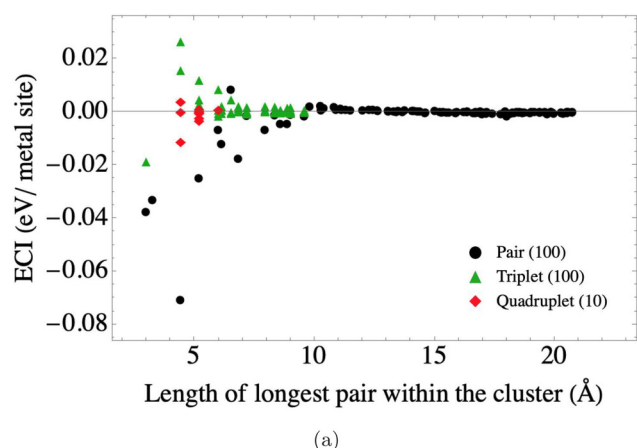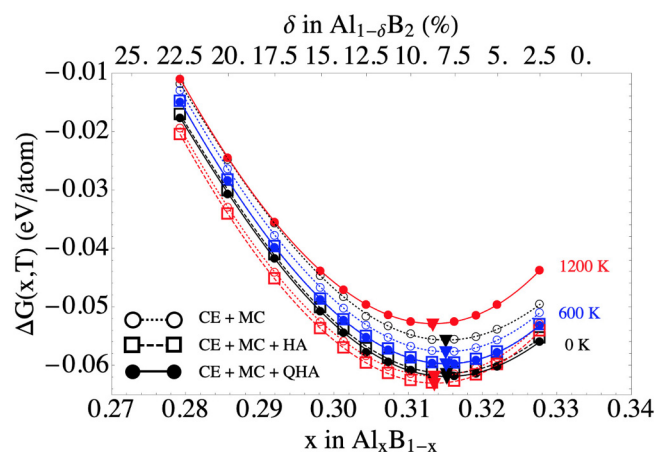

(a)

(b)

FIG. 10. Cluster expansion properties. (a) Effective cluster interactions as a function of length of the longest pair within the cluster. In brackets are the number of n-site clusters. (b) Fitted (in blue) and predicted (in red and green for randomly excluded structures) CE formation energies vs calculated DFT values.

FIG. 11. Gibbs free energy of formation $\Delta G(x, T)$ [Eq. (6)] of Al_xB_{1-x} structures at $T = 0, 600,$ and 1200 K. The curves are obtained from MC simulations (open circles and dotted lines), with the addition of vibrations in HA (open squares and dashed lines) and QHA (solid circles and solid lines). The minimum of each curve is marked by triangles.

0 K (black), 600 K (blue), and 1200 K (red) based on

$$\Delta G(x, T) = \Delta F_{\text{conf}}^{\text{MC}}\left(\delta = \frac{3x - 1}{x - 1}, T\right) + \Delta F_{\text{vib}}^{\text{(Q)HA}}(x, T). \quad (6)$$

The first is purely configurational (open circles and dotted lines) taken directly from the MC simulations, the second being configurational + HA (open squares and dashed lines), and the third is configurational + QHA (solid circles and solid lines). In the HA, vibrational contributions to the free energy are negative for all considered temperatures, while in QHA the $\Delta F_{\text{vib}}^{\text{QHA}}(x, T)$ term turns positive at 1000 K and above, effectively destabilizing the system. This is readily observed at 1200 K marked by the red curves, where the HA curve sits below the purely configurational one, while the QHA curve lies above both of the two other approximations. This is due to thermal expansion outbalancing the other configurational and vibrational effects. Within each approximation, the minimum of $\Delta G(x, T)$, marked by triangles, does not notably shift toward higher or lower aluminum content with increasing temperature. This means vacancy concentrations that are stable at low temperature likely remain stable up to structural decomposition. When comparing in-between the three approximations, at any fixed temperature, the apparent effect of vibrations is largely only a vertical shift in the free energy and is thus not expected to considerably affect phase stability.

To investigate this matter further and capture the evolution of phase stability of Al_xB_{1-x} with temperature, common tangent construction is applied to $\Delta G(x, T)$ curves at a set of fixed temperatures. This derives the $T - x$ phase diagram of Al_xB_{1-x} and is shown in Fig. 12.

For a given temperature, the common tangent compositions that Al_xB_{1-x} share with fcc-Al and α-B, respectively, are marked by
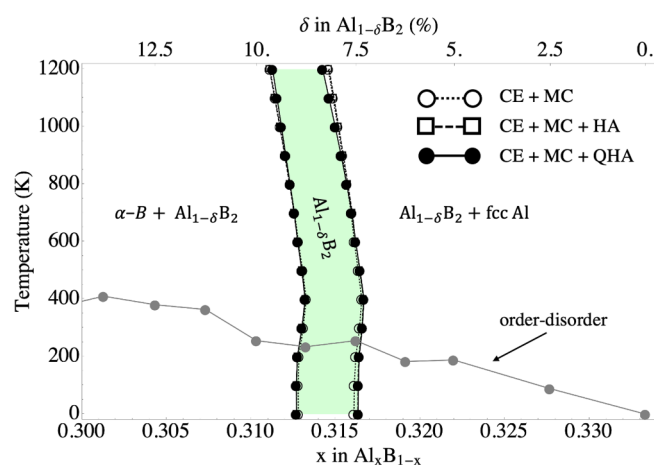

FIG. 12. Phase diagram of Al_xB_{1-x} predicting a narrow stability region (green area spanned by CE + MC + QHA), outside which the compound faces decomposition. Level of approximation is given by the different symbols in the legend. The compositional dependent order–disorder transition temperature is given by the gray circles.

black symbols in Fig. 12. The green area, which is spanned by the quasiharmonic points, corresponds to the region where Al_xB_{1-x} is stable and exists as a single-phase solid solution. Outside in the white regions, the compound faces decomposition into a mixture of either Al-rich or B-rich phases of different structures together with $Al_{1-\delta}B_2$. For each composition, the vacancy order–disorder transition temperature is determined by the position of the heat capacity peak and is here marked by the gray circles. Within the stability window, below 200 K, the vacancies are predicted to be ordered. Thus, in the more relevant temperature region at and above room temperature, any vacancies are predicted to be disordered. One can notice the close matching of HA (open squares) and QHA (solid circles) with static lattice approximation (open circles), derived directly from the CE approach and MC simulations. This suggests that vibrational contributions to configurational ΔG_{form} in both HA and QHA are not likely to have distinct impact on overall phase stability. This can be understood from the view that the energetic contribution from the thermal expansion of the defective phases is balanced by those of the constituent elements (pure Al and B). In other words, phase stability is seemingly dictated by the atomic configuration on the metal sublattice, leading to electronic structure effects discussed in Sec. III A. Based on the extreme points of the CE + MC + QHA approach, regardless of temperature, the stability window of $Al_{1-\delta}B_2$ is predicted to be bounded within the narrow range $0.073 \leq \delta \leq 0.096$, which corresponds to $0.311 \leq x \leq 0.317$ in the formulation of Al_xB_{1-x}.

It is worthwhile to point out that in Figs. 11 and 12, we go beyond the melting temperature of pure aluminum (933 K) and come close to the lowest reported decomposition temperature of AlB_2 (1253–1928 K[44–48]). In the upper temperature region, close to melting, phonon–phonon interactions become increasingly important. One limitation of QHA is that they are not covered in its description. In the work of Glensk et al.,[49] they investigated how anharmonicity affects vacancy formation energy in elemental fcc-Al and Cu, using other ab initio techniques, which was found to have a considerable impact at temperatures above 55% T_{melt}. At T_{melt}, the addition of anharmonicity to vibrations on the quasiharmonic level effectively shifts the formation energy by 10% for Al and 25% Cu.[49]

In this study, even if such anharmonic effects are not explicitly treated, they were explored on a best-effort basis, in which they were introduced into our model as a temperature dependent amplification to the QHA contribution. We acknowledge that our binary system may give rise to more complex phonon–phonon interplay, and direct comparisons with results related to fcc structures in the work of Glensk et al. is difficult. However, our best-effort estimation indicates that anharmonic contributions, with analogous impact on the formation energy, do not appreciably affect phase stability in our system.

Furthermore, through private communications with the group of Körmann of the Max-Planck-Institut für Eisenforschung and Technische Universiteit Delft, we obtained the DFT-calculated free energies of fcc and liquid Al with anharmonic corrections which underly the results in Refs. 50–52. Phase stability with these as competing phases, and not only quasiharmonic fcc-Al and α-B, was investigated. However, the phase diagram was again found to only be slightly affected, narrowing the stability window above 1000 K. This narrowing effect is most pronounced at 1200 K using liquid Al as a competing phase. Yet, the phase diagram boarder

points x_1 and x_2 of Al_xB_{1-x} are shifted less than 0.2%. Thus, it is concluded that phase stability of Al_xB_{1-x} is predominantly determined by configurational thermodynamics.

D. Thermal expansion

In our static DFT calculations for ideal vacancy-free AlB_2, we obtain $a = 3.01\,\text{Å}$ and $c = 3.29\,\text{Å}$. At room temperature in the QHA, we obtain $a = 3.02\,\text{Å}$ and $c = 3.31\,\text{Å}$, which can be compared to the room temperature experimental measurements in the literature of $a_{lit}^{exp}(298) = 3.003(1),$ [53] $3.009(1),$ [54] $3.0050(1)\,\text{Å}$ [18] and $c_{lit}^{exp}(298) = 3.254(1),$ [53] $3.262(1),$ [54] $3.2537(8)\,\text{Å}.$ [18] One does expect a small overestimation of lattice spacing in GGA-based DFT calculations. As a comparison, we obtain $a = 4.07\,\text{Å}$ for pure fcc-Al in the QHA at room temperature, with the experimental value being $4.05 \pm 0.0006\,\text{Å}.$ [54] For α-B, we get $a = 5.07$ in the QHA at 298 K, while experiments show $a = 5.0623(3)\,\text{Å}.$ [55] The overestimation for fcc-Al and α-B is 0.49% and 0.15%, respectively. For stoichiometric AlB_2, the overestimation is, on average, 0.50% for a and 1.64% for c. Meanwhile, for the isostructural diboride TiB_2, a similar comparison between experiments and theory on the quasiharmonic level using GGA yields an overestimation of only 0.40% and 0.39% for the a and c lattice parameters, respectively. [10]

Thus, it becomes apparent that the calculated c-parameter of AlB_2 is overestimating the experiment more than expected. This is an indication of the importance of metal vacancies on the structural parameters of the phase. The theoretical thermal expansion of lattice parameters a and c of stoichiometric AlB_2, ordered and disordered metal deficient $Al_{1-\delta}$ structures, and our experimental measurements are presented in Fig. 13.

Ideal stoichiometric AlB_2 is shown in green. $Al_{11}B_{24}$, the structure in the middle of Fig. 5(b), with ordered Al vacancies is shown in orange. The manually created structure Al_7B_{16} with 12.5% ordered Al vacancies [discussed in Figs. 2(b) and 4] that are situated in alternating Al layers is shown in gray. Here, these three structures are presented semitransparent as the phase diagram predicts that *ordered* vacancy structures are of lesser importance than *disordered* at and above room temperature, where the experimental measurements are performed.

The two disordered SQSs with 10% and 12.5% vacancies are shown in black and red, respectively. For all vacancy structures, the lattice parameters were derived as averages of nearest-neighboring ab-plane (for a) and interplanar (for c) distances for all pairs of boron atoms. The experimental values of the lattice parameters, obtained from *in situ* XRD measurements during heating, are shown in blue. At room temperature, we find $a(298) = 3.0062(11)\,\text{Å}$ and $c(298) = 3.2532(37)\,\text{Å}$. This is closely matching previously mentioned values from the literature, here represented by purple open squares. Our experimental lattice parameters can be fitted using least squares weighted with the experimental error bars to the following expression, shown with dashed blue lines in the figure:

$$a = 3.002 + 1.281 \times 10^{-5}\,T + 2.714 \times 10^{-9}\,T^2 (\text{Å}),$$

$$c = 3.243 + 3.623 \times 10^{-5}\,T - 1.540 \times 10^{-9}\,T^2 (\text{Å}), \quad (7)$$
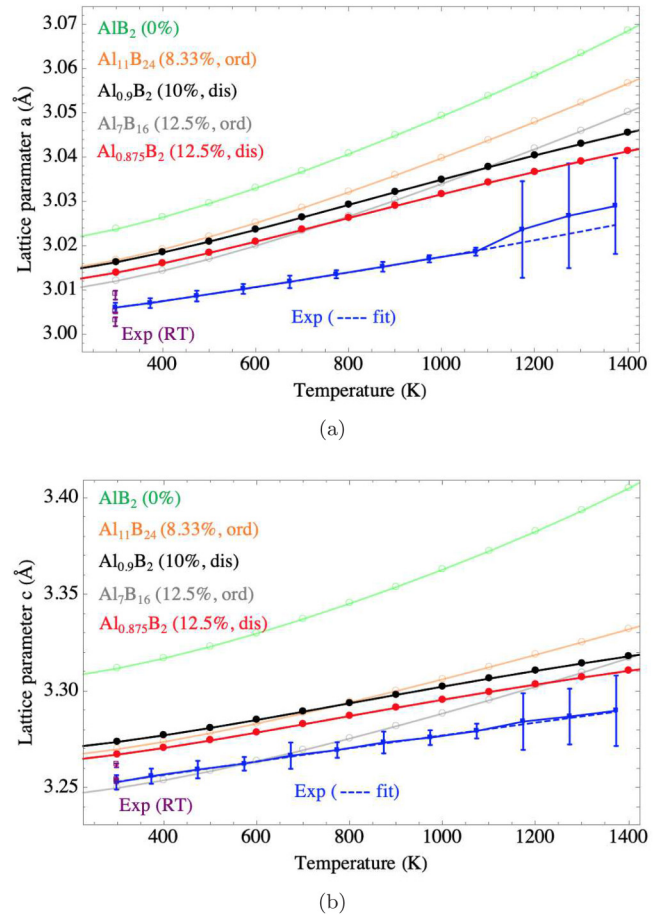

(a)

(b)

FIG. 13. Thermal expansion of stoichiometric and metal deficient AlB_2, with Al-vacancy concentration and order or disorder index in parentheses. In blue squares are our measured *in situ* XRD values, with experimentally fitted dashed lines corresponding to Eq. (7). Purple open squares correspond to experimental reference values at room temperature. [17,18,53] Colored (open) circles are the values obtained from our DFT calculations. (a) Lattice parameter a. (b) Lattice parameter c.

where $298\,\text{K} \leq T \leq 1373\,\text{K}$. From these fits, the experimental linear thermal expansion coefficients at 298 K take the values $\alpha_a^{exp}(298) = 4.80 \times 10^{-6}\,\text{K}^{-1}$ and $\alpha_c^{exp}(298) = 10.85 \times 10^{-6}\,\text{K}^{-1}$. The linear thermal expansion coefficients are calculated for ideal

TABLE I. Linear thermal expansion coefficients at 298 K.

Composition	Method	$\alpha_a(\times 10^{-6}\,\text{K}^{-1})$	$\alpha_c(\times 10^{-6}\,\text{K}^{-1})$
AlB_2 [a]	Expt.	4.80	10.85
AlB_2	Calc.	8.02	12.58
$Al_{11}B_{24}$	Calc.	8.41	12.59
$Al_{0.90}B_2$	Calc.	8.64	12.44
$Al_{0.875}B_2$	Calc.	9.49	11.96

[a]Nominal composition of commercially available powder.

stoichiometric AlB_2, ordered $Al_{11}B_{24}$, and the two disordered SQS $Al_{0.90}B_2$ and $Al_{0.875}B_2$. For easy comparison, the values are presented in Table I.

However, the difference in thermal expansion is most pronounced at elevated temperatures, above 1000 K, and it is also fruitful to compare the temperature trends. One way to capture the expansivity of the lattice parameters we obtain experimentally is to calculate the absolute change. We find that the increase in a from 298 to 1373 K via $a^{exp}(1373)/a^{exp}(298)$ is 0.76% and 1.14% for c. In contrast, ideal AlB_2 expands 1.43% and 2.71% in a and c, respectively. For the ordered ground state structure $Al_{11}B_{24}$, the expansions are 1.28% and 1.84%. As hinted by the red and black curves in Fig. 13, the two disordered vacancy structures capture the trend very well. For $Al_{0.90}B_2$ (black), the a parameter increases by 0.95% and the c parameter by 1.32%. The closest match to experiments is obtained by $Al_{0.875}B_2$ (red) with a corresponding increase of 0.89% and 1.30%. This further demonstrates the increased importance of Al vacancies when comparing the lattice parameters as a function of temperature.

There are two main takeaways from the curves presented in Fig. 13: First, the results suggest that the absolute values of both lattice parameters depend on the vacancy concentration. An increasing amount of vacancies leads to a decrease in both a and c, most notably for the latter. Second, the temperature trend of the lattice expansion is dependent on the vacancy configuration. The best agreement with the experiment (blue) is obtained by the disordered SQS (red) structure of Al vacancies, indicating that vacancies are indeed present in the sample and take on a disordered configuration, in accord with the findings from the phase diagram in Fig. 12.

IV. CONCLUSION

We have used electronic structure theory and alloy theory based first-principles simulations to investigate the phase stability, configurational properties, and temperature dependence of lattice parameters of metal deficient $Al_{1-\delta}B_2$. We complement the theoretical calculations with experimental measurements of the thermal expansion of $Al_{1-\delta}B_2$ powders using *in situ* XRD. Our calculations reveal the following:

(i)   Out of various investigated defects, only Al vacancies are shown to be stable.

(ii) Stoichiometric ideal AlB_2 is not stable with respect to Al-vacancy formation and pure Al at any temperature.

(iii) The formation of vacancies within the aluminum layers deplete filled antibonding Al-s character orbitals in the conduction band near the Fermi level as has been explicitly shown in electronic DOS calculations.

(iv) At low temperature, three structures with ordered Al vacancies, with 7.69%, 8.33%, and 10% vacancies and formula $Al_{12}B_{26}$, $Al_{11}B_{24}$, and Al_9B_{20}, respectively, are found to be stable and lie on the 0 K convex hull. They all display Al vacancies ordered along lines in the Al layers.

(v)   Ordered structures are predicted to be stable up to around 200 K, above which the vacancies' disorder highlights the relevance of a disordered state in applications at and above room temperature.

(vi) Phase stability criteria based on canonical MC simulations of the configurational free energy curves, with addition of vibrational-free energies, reveal a very narrow stability range for Al_xB_{1-x} structures. At 0 K, the stability range is $0.313 \leq x \leq 0.316$ ($0.076 \leq \delta \leq 0.089$), which is then shifted to $0.313 \leq x \leq 0.317$ ($0.072 \leq \delta \leq 0.089$) at room temperature and $0.311 \leq x \leq 0.314$ ($0.085 \leq \delta \leq 0.097$) at 1200 K, close to the decomposition temperature. This narrowness is explained by electron structure effects driven by metal vacancies that are favorable only in a small concentration window. The energetically beneficial depletion of antibonding states is quickly followed by the depletion of bonding states if the vacancy concentration exceeds 12%.

(vii) The effect of adding lattice dynamics on a quasiharmonic level to the free energy of metal deficient phases has been investigated. The respective energetic contribution is largely canceled when compared with those of the constituent pure elements. Therefore, thermal expansion found to not have a significant impact on the phase diagram of this system.

(viii) Our calculated narrow stability range of $Al_{1-\delta}B_2$ and its origin in the electronic structure can reconcile the experimental Al–B phase diagrams that typically show a line compound of AlB_2 type with the known existence of the phase off-stoichiometry, that in other systems often result in a broader composition range of stability.

(ix) The effect of vacancy configuration and concentration on lattice dynamics and thermal expansion has been investigated. It is found that the absolute values of both a and c lattice parameters decrease with increasing vacancy concentration. Furthermore, disordered vacancies lead to a stiffer lattice and lower thermal expansion, as compared to ordered vacancies. This is in close agreement with the temperature trend of measured lattice parameters in our experiments that give linear thermal expansion coefficients of $\alpha_a^{exp}(298\,K) = 4.80 \times 10^{-6}$ K^{-1} and $\alpha_c^{exp}(298\,K) = 10.85 \times 10^{-6}\,K^{-1}$.

DATA AVAILABILITY

The data that support the findings of this study are available from the corresponding author upon reasonable request.

REFERENCES

[1] J. Nagamatsu, N. Nakagawa, T. Muranaka, Y. Zenitani, and J. Akimitsu, Nature 410, 63 (2001).

[2] C. Buzea and T. Yamashita, Supercond. Sci. Technol. 14, R115 (2001).

[3] V. I. Matkovich, Boron and Refractory Borides (Springer Verlag, New York, 1977).

[4] R. G. Munro, J. Res. Natl. Inst. Stand. Technol. 105, 709 (2000).

[5] E. Wuchina, E. Opila, M. Opeka, W. Fahrenholtz, and I. Talmy, Electrochem. Soc. Interface 16, 30–36 (2007).

[6] W. G. Fahrenholtz, G. E. Hilmas, I. G. Talmy, and J. A. Zaykoski, J. Am. Ceram. Soc. 90, 1347 (2007).

[7] L. Tengdelius, J. Birch, J. Lu, L. Hultman, U. Forsberg, E. Janzén, and H. Högberg, Phys. Status Solidi A 211, 636 (2014).

[8] X. M. Wang, J. Alloys Compd. 403, 283 (2005).

[9] B. Alling et al., Sci. Rep. 5, 9888 (2015).

[10] E. Johansson, A. Ektarawong, J. Rosen, and B. Alling, J. Appl. Phys. 128, 235101 (2020).

[11] A. Mockute et al., Scr. Mater. 127, 122 (2017).

[12] A. Mockute et al., Thin Solid Films 669, 181 (2019).

[13] I. Loa, K. Kunc, K. Syassen, and P. Bouvier, Phys. Rev. B 66, 134101 (2002).

[14] V. I. Matkovich, J. Economy, and J. R. F. Giese, J. Am. Chem. Soc. 86, 2337 (1964).

[15] J. Nakamura, M. Watanabe, T. Oguchi, S. Y. Nasubida, E. Kabasawa, N. Yamada, K. Kuroki, H. Yamazaki, S. Shin, Y. Umeda et al., J. Phys. Soc. Jpn. 71, 408 (2002).

[16] T. Sun, Y. G. Zhao, R. Fan, X. P. Zhang, B. G. Liu, Y. H. Xiong, and P. J. Li, J. Supercond. Incorporat. Novel Magn. 17, 473 (2004).

[17] M. Merz, P. Schweiss, T. Wolf, H. von Löhneysen, and S. Schuppler, J. Phys. Soc. Jpn. 83, 024714 (2014).

[18] U. Burkhardt, V. Gurin, F. Haarmann, H. Borrmann, W. Schnelle, A. Yaresko, and Y. Grin, J. Solid State Chem. 177, 389 (2004).

[19] K. Koch, Ph.D. dissertation, Fakultät Mathematik und Naturwissenschaften der Technischen Universität Dresden, 2009.

[20] O. N. Carlson, Bull. Alloy Phase Diagrams 11, 560 (1990).

[21] G. Kresse and J. Furthmüller, Phys. Rev. B 54, 11169 (1996).

[22] G. Kresse and D. Joubert, Phys. Rev. B 59, 1758 (1999).

[23] P. Blöchl, Phys. Rev. B 50(24), 17953 (1994).

[24] J. Perdew, K. Burke, and M. Ernzerhof, Phys. Rev. Lett. 77, 3865 (1996).

[25] H. J. Monkhorst and J. D. Pack, Phys. Rev. B 13, 5188 (1976).

[26] F. Birch, Phys. Rev. 71(11), 809 (1947).

[27] F. D. Murnaghan, Proc. Natl. Acad. Sci. U.S.A. 30, 244 (1944).

[28] P. Blöchl, O. Jepsen, and O. K. Andersen, Phys. Rev. B 49, 23 (1994).

[29] A. Zunger, S.-H. Wei, L. G. Ferreira, and J. E. Bernard, Phys. Rev. Lett. 65(3), 353 (1990).

[30] J. M. Sanchez, F. Ducastelle, and D. Gratias, Physica A 128, 334 (1984).

[31] J. W. Connolly and A. R. Williams, Phys. Rev. B 27, 5169 (1983).

[32] A. van de Walle, M. Asta, and G. Ceder, Calphad 26, 539 (2002).

[33] G. L. W. Hart and R. W. Forcade, Phys. Rev. B 77, 224115 (2008).

[34] A. van de Walle and G. Ceder, J. Phase Equilib. 23, 348 (2002).

[35] A. van de Walle and M. Asta, Modell. Simul. Mater. Sci. Eng. 10, 521 (2002).

[36] A. Togo and I. Tanaka, Scr. Mater. 108, 1 (2015).

[37] P. Brüesch, Phonons: Theory and Experiments I (Springer, Berlin, 1982).

[38] G. Leibfried and W. Ludwig, Solid State Phys. 12, 275 (1961).

[39] B. Fultz, Prog. Mater. Sci. 55, 247 (2010).

[40] K. Parlinski, Z. Q. Li, and Y. Kawazoe, Phys. Rev. Lett. 78, 4063 (1997).

[41] T. J. B. Holland and S. Redfern, Mineral. Mag. 61, 65 (1997).

[42] A. Jain, S. P. Ong, G. Hautier, W. Chen, W. D. Richards, S. Dacek, S. Cholia, D. Gunter, D. Skinner, G. Ceder et al., APL Mater. 1, 011002 (2013).

[43] X. Vajeeston, P. Ravindran, C. Ravi, and R. Asokamani, Phys. Rev. B 63, 045115 (2001).

[44] X. Wang, J. Alloys Compd. 403, 283 (2005).

[45] L. F. Mondolfo, Aluminium Alloy Structure and Properties (Butterworth, London, 1976).

[46] A. Hall and J. Economy, J. Phase Equilib. 21–1, 63 (2000).

[47] N. Mahallawya, M. A. Taha, A.E.W. Jarfors, and H. Fredriksson, J. Alloys Compd. 292, 221 (1999).

[48] A. A. Giardini, J. A. Kohn, L. Toman, and D. W. Eckart, Boron-Synthesis, Structure and Properties (Plenum Press, New York, 1960).

[49] A. Glensk, B. Grabowksi, T. Hickel, and J. Neugebauer, Phys. Rev. X 4, 011018 (2014).

[50] B. Grabowksi, L. Ismer, T. Hickel, and J. Neugebauer, Phys. Rev. B 79, 134106 (2009).

[51] L.-F. Zhu, B. Grabowksi, and J. Neugebauer, Phys. Rev. B 96, 224202 (2017).

[52] L.-F. Zhu, J. Janssen, S. Ishibashi, F. Körmann, B. Grabowksi, and J. Neugebauer, Comput. Mater. Sci. 187, 110065 (2021).

[53] E. J. Felten, J. Am. Chem. Soc. 78, 5977 (1956).

[54] P. N. Nakashima, The Crystallography of Aluminum and Its Alloys (CRC Press, 2018), Chap. 31, https://www.routledgehandbooks.com/doi/10.1201/9781351045636-140000245.

[55] K. A. Cherednichenko and V. L. Solozhenko, Solid State Commun. 303–304, 113735 (2019).